RSC Advances

PAPER

View Article Online
View Journal | View Issue

Cite this: *RSC Adv.*, 2021, **11**, 9296

Synthesis of $ZnIn_2S_4$@Co_3S_4 particles derived from ZIF-67 for photocatalytic hydrogen production†

Ganyu Wang,[ab] Wenqian Chen,[*ab] Yu Zhang,[ab] Qinshang Xu,[ab] Yirui Li,[ab] Maw Lin Foo[c] and Liang Tang[*ab]

Received 24th December 2020
Accepted 19th February 2021

DOI: 10.1039/d0ra10799a

rsc.li/rsc-advances

In this work, ZIF-67 derivative Co_3S_4 with diamond dodecahedron structure was firstly synthesized *via* a series of reactions, and $ZnIn_2S_4$@Co_3S_4 heterostructures with adjustable band gaps were successfully obtained through a simple hydrothermal method. Consequently, $ZnIn_2S_4$@Co_3S_4 heterostructures have significantly enhanced visible light absorption and improved photocatalytic efficiency, among which the ZC-5 composite exhibits the highest photocatalytic hydrogen production rate up to 4261 μmol g^{-1} h^{-1} under simulated sunlight, to be approximately 4.8 times higher than that of pure $ZnIn_2S_4$. The enhanced photocatalytic activity can be attributed to faster electron transfer and more efficient electron–hole pairs separation derived from the heterostructures which form at the interface between Co_3S_4 and $ZnIn_2S_4$. Thus, this study provides a good strategy for photocatalytic hydrogen production without precious metals using heterostructures.

1. Introduction

Due to increasingly serious environmental pollution caused by the burning of fossil fuels and the increasing global demand for energy, it is necessary to explore a clean and renewable alternative.[1,2] Hydrogen energy generated by simulated solar photocatalysis reaction is an effective means to solve the current problem.[3,4] In 1972, Fujishima *et al.* discovered that water could be decomposed into hydrogen under ultraviolet light by photoelectrochemical technology with the help of titania.[5] Since then, photocatalysts based on semiconductor materials for hydrogen production utilizing solar energy have been widely studied.[6] So far, researchers have invented and developed various photocatalysts that respond to visible light, such as oxides (ZnO[7]), nitride (g-C_3N_4 (ref. 8)), and sulfides (CdS,[9] MoS_2 (ref. 10)).

Zinc indium sulfide ($ZnIn_2S_4$), as a ternary metal chalcogenide, is considered as a prominent photocatalyst due to its suitable band gap, good visible light response, environmental friendliness and relatively excellent chemical stability.[11] In recent years, $ZnIn_2S_4$ has been widely applied in photocatalytic hydrogen production,[12] carbon dioxide reduction,[13] dye degradation[14] and so on. However, for photocatalytic hydrogen evolution, $ZnIn_2S_4$ still faces some challenges to increase the activity, such as how to enhance the response of visible light and improve the transfer and separation efficiency of photogenerated charge carriers. A number of strategies have been explored to modify $ZnIn_2S_4$ for potential practical applications including structure and morphology controlling (nanoparticle,[15] nanosheets,[16] microsphere[17]), element doping (copper,[18] nitrogen,[19] alkaline-earth metal[20]), co-catalyst modifying (Au@Pt,[21] WS_2,[22] MoS_2 (ref. 23)) and heterojunction construction (CeO_2/$ZnIn_2S_4$,[24] ZnS/$ZnIn_2S_4$ (ref. 25)). For example, Shen *et al.*[26] reported that hexagonal $ZnIn_2S_4$ photocatalysts with different crystallinity and morphology were synthesized under different mediated conditions, exhibiting different photocatalytic properties. Shen *et al.*[18] prepared a series of $ZnIn_2S_4$ doped with different amounts of copper with improved photocatalytic activity. An *et al.*[21] designed a novel $ZnIn_2S_4$ which loaded core–shell Au@Pt on nanosheets surface, showing outstanding visible hydrogen production ability. However, high prices, poor durability and low abundance limit the use of precious metals on a large scale. Among all the modifications, it is preferable to build heterojunction structures by integrating $ZnIn_2S_4$ with other semiconductors without noble metals, which could stagger the arrangement of energy levels, thus accelerating charge separation and transmission.

As an emerging porous crystal materials, metal–organic frameworks (MOFs) consisted of metal units and organic ligands have an advantage in large surface areas, adjustable pore sizes and myriad of crystal structures, which can supply abundant active sites and promote charge transfer.[27] However, MOFs are not ideal in terms of cyclic stability and still need to be modified.[28] At present, MOFs have been widely used as precursors or templates to prepare functional materials with

[a]*Key Laboratory of Organic Compound Pollution Control Engineering, Ministry of Education, Shanghai University, Shanghai 200444, PR. China*
[b]*School of Environmental and Chemical Engineering, Shanghai University, Shanghai 200444, PR China. E-mail: wenqianchen@shu.edu.cn; tang1liang@shu.edu.cn*
[c]*Department of Chemistry, National University of Singapore, 117543, Singapore*

† Electronic supplementary information (ESI) available. See DOI: 10.1039/d0ra10799a

specific components and complex structures, such as porous carbon materials,[29] metal oxides[30] and metal sulfides.[31] Meanwhile, this process is easily achieved by means of hydrothermal or calcination. The obtained functional materials continue the virtues of MOFs and exhibit superior performance.[32,33] Moreover, when the energy band structures of the two components are well matched, MOF derivatives can promote electron transfer and photo-generated charge carrier separation through contact surfaces to improve activity.[34,35] Therefore, MOF derivatives are widely applied in environmental energy catalysis.

Therefore, in this study, a novel $ZnIn_2S_4$@Co_3S_4 composite photocatalyst based on ZIF-67 derivative is reported. First, ZIF-67 is converted into Co_3S_4 by two-step method, and then $ZnIn_2S_4$ nanosheets are grown on the surface of Co_3S_4 in the hydrothermal process, forming heterogeneous structures between $ZnIn_2S_4$ and Co_3S_4, which promote charge transfer and separation. As expected, the fabricated $ZnIn_2S_4$@Co_3S_4 composite photocatalysts show better photocatalytic hydrogen production performance compared with $ZnIn_2S_4$. Moreover, the effects of different coupling amount of Co_3S_4 on the photocatalytic hydrogen production performance are studied. In addition, according to the $ZnIn_2S_4$@Co_3S_4 energy level structure, a possible photocatalytic hydrogen evolution mechanism is proposed.

2. Experimental section

2.1. Chemicals

Cobalt nitrate hexahydrate ($Co(NO_3)_2 \cdot 6H_2O$, RG), indium chloride tetrahydrate ($InCl_3 \cdot 4H_2O$, RG), thioacetamide (TAA, RG), 2-methylimidazole (2-MeIM, RG), triethanolamine (TEOA) were all obtained from Titan Technology. Zinc nitrate hexahydrate ($Zn(NO_3)_2 \cdot 6H_2O$, RG) was purchased from Sinopharm Chemical Reagent Co. Ltd. All chemicals and materials were used directly without further purification.

2.2. Synthesis of $ZnIn_2S_4$@Co_3S_4 hollow composites

Co_3S_4 was synthesized according to a modified method reported in the literature.[36] It can be divided into three parts. Firstly, the synthesis of ZIF-67, 2-methylimidazole (7.88 g) was dissolved in 60 mL of methanol to form a transparent solution, which was quickly poured into another 60 mL of methanol solution dissolving $Co(NO_3)_2 \cdot 6H_2O$ (3.48 g), and the mixture was stirred vigorously for 1 min. Then, the mixture was kept at room temperature for 24 h. The purple precipitation was obtained by centrifugation, washed at least three times and vacuum dried at 60 °C for 12 h. Secondly, 80 mg of ZIF-67 was dispersed in 20 mL of absolute ethanol by ultrasound for 20 min. Then another 20 mL solution of absolute ethanol containing TAA (0.12 g) was added. Thereafter, the mixture was transferred to a 50 mL Teflon-lined stainless-steel autoclave and reacted at 120 °C for 4 h. The hollow Co_3S_4 was obtained by centrifugation, washing and drying. Finally, they were annealed in N_2 atmosphere at 350 °C for 2 h with a heating rate of 1 °C min^{-1}.

$ZnIn_2S_4$@Co_3S_4 nanocomposites were prepared by a simple hydrothermal reaction. The Co_3S_4 content is 2%, 5%, 10%, 20% respectively and they were labeled as ZC-*X* (*X* = the percentage of Co_3S_4). In a typical experimental procedure, a certain amount of Co_3S_4, 1.0 mmol $Zn(NO_3)_2 \cdot 6H_2O$ (0.297 g), 2.0 mmol $InCl_3 \cdot 4H_2O$ (0.586 g) and 6.0 mmol TAA (0.45 g) was dissolved in 60 mL deionized water and evenly dispersed by stirring for 60 min. After that, the mixture was transferred to a 100 mL Teflon-lined stainless-steel autoclave and reacted at 160 °C for 12 h. Finally, the sediment was separated by centrifuge, washed with deionized water and absolute ethanol at least three times and dried under vacuum overnight at 60 °C. The above synthesis process is shown in Scheme 1. To make comparisons, the pure $ZnIn_2S_4$ was synthesized at the same reaction condition without Co_3S_4.

2.3. Materials characterization

An X-ray diffractometer (Bruker D8 Advance XRD) was used to characterize the crystal structure of the synthesized samples by Cu Kα radiation operated at 40 kV and 40 mA in the range of 5° to 80°. The morphologies and microstructures of prepared photocatalysts were observed by scanning electronic microscopy (Gemini SEM300), operating at 15 kV equipped with energy-dispersive X-ray spectra (EDS). The elemental composition and valence of sample surface were obtained by K-Alpha + X-ray photoelectron spectrometer (XPS) with mono Al Kα radiation. Ultraviolet-visible (UV-vis) diffuse reflectance spectra (DRS) of prepared samples were performed by an UV-vis spectrophotometer (UV-2600, Shimadzu, Japan) with the background of $BaSO_4$. The photoluminescence (PL) spectra were measured by Gangdong Technology F-320 PL spectrophotometer with the excitation wavelength of 260 nm. BeiShiDe Micropore Analyzer 3H-2000PM were employed to test the Brunauer–Emmett–Teller (BET) surface areas of the samples.

2.4. Photoelectrochemical properties measurements

The electrochemical workstation (CHI660E Instruments) was used to analyze the photoelectrochemical properties of the obtained samples by amperometric *i–t* curves and electrochemical impedance spectroscopy (EIS) and Mott–Schottky analysis. The tests were carried out with a conventional three-electrode system consisting of platinum-sheet electrode, saturated calomel electrode (SCE) and conductive glass coated with sample powder, which served as counter electrode, reference electrode and working electrode, respectively. The working electrode was prepared by a method which is similar to the literature reported by Ling *et al.*[37] The *ca.* 10 mg catalyst and 5 w% solution of polyvinylidene fluoride in *N*-methyl pyrrolidone solution were fully grinded in a ratio of 9 : 1, and then coated on the conductive surface of conductive glass for vacuum drying at

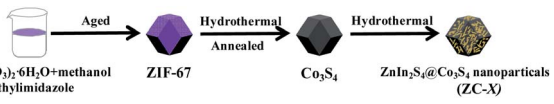

Scheme 1 Schematic of the synthesis of the $ZnIn_2S_4$@Co_3S_4 nanocomposites.

60 °C for 12 h. Meanwhile, 0.5 M Na_2SO_4 solution was used as the electrolyte. The amperometric *i–t* curves was tested by the intermittent irradiation of a 300 W Xe lamp (CEL-HXF300). An impedance-potential model was applied to the Mott–Schottky measurement, where the voltage range was −1.5 to 1.5 V. The EIS tests were done in a dark condition with a frequency ranging from 10^{-2} and 10^5 Hz.

2.5. Photocatalytic H_2 production experiments

The photocatalytic hydrogen production reactions were carried out in a 250 mL closed quartz glass reactor, which was irradiated by a 300 W Xe lamp (PLS-SXE 300, Perfectlight, Beijing, $\lambda \geqq 350$ nm). Generally, 40 mg of photocatalyst was dispersed into 60 mL homogeneous solution containing 50 mL deionized water and 10 mL TEOA as sacrificial agent with constantly stirring. Before the photocatalytic reaction, the gas in the system was completely evacuated and the temperature of hydrogen production reaction was controlled at 5 °C by a cold-water circulation system. The photocatalytic hydrogen evolution rate was collected by a Shimadzu GC-2014C gas chromatograph.

3. Results and discussions

3.1. Structures and compositions

The X-ray diffraction (XRD) patterns of pure $ZnIn_2S_4$ and ZC-*X* (*X* = 2–20) composites with different proportions of Co_3S_4 are shown in Fig. 1. The characteristic peaks of prepared pure $ZnIn_2S_4$ are present at 21.6°, 27.7°, 39.9°, 47.2°, 52.4° and 55.6°, which is consistent with (006), (102), (108), (110), (116), and (202) crystal planes matching hexagonal $ZnIn_2S_4$ (JCPDS no. 65-2023).[38] Meanwhile, ZIF-67 as a sacrifice template is successfully synthesized which can be proved by XRD (Fig. S1a†). The diffraction peak of Co_3S_4 is displayed in Fig. S1b,† and the corresponding position of each peak is in accordance with that in the literature.[39] All diffraction peaks of ZC-*X* composites are the same as that of pure $ZnIn_2S_4$, and it can be seen that a gradual decrease in the peak intensity of $ZnIn_2S_4$ with the increasing incorporating amount of Co_3S_4, which signifies the formation of a heterojunction between $ZnIn_2S_4$ and Co_3S_4. However, no diffraction peak of Co_3S_4 is found in ZC-*X*, because the crystallinity of Co_3S_4 is much lower than that of $ZnIn_2S_4$ (Fig. S1b†) and Co_3S_4 has a relatively small amount and high dispersion in the ZC-*X* composites. The presence of Co_3S_4 in ZC-*X* composites is further confirmed by SEM, TEM and XPS characterization tests.

The morphology of the synthesized samples and intimate contact between $ZnIn_2S_4$ and Co_3S_4 are observed by transmission electron microscopy (TEM) and scanning electron microscopy (SEM). The particle of ZIF-67 is hollow diamond dodecahedron with smooth surface and regular shape (Fig. S2a†). Meanwhile, as shown in Fig. 2a and S2b,† pure Co_3S_4 still retains the initial hollow diamond dodecahedron shape of the ZIF-67 with relatively smooth surface, and the TEM image is relatively transparent due to the hollow structure. Fig. 2b and S2c† shows that pure $ZnIn_2S_4$ is a solid microsphere structure composed of nanosheets. Compared with pure Co_3S_4, it can be seen from Fig. 2d and e that the surface of ZC-5 composites becomes rougher. Meanwhile, Fig. 2c displays the TEM image of ZC-5 which further confirms that $ZnIn_2S_4$ nanosheets grow on the surface of the hollow structure of Co_3S_4, indicating that $ZnIn_2S_4$ successfully compound with Co_3S_4 and there are a clear interaction between $ZnIn_2S_4$ and Co_3S_4. The coupling of Co_3S_4 effectively inhibits the aggregation of $ZnIn_2S_4$ nanocrystals, which is beneficial to increase the active site of photocatalysis. Additionally, the EDS spectra of ZC-5 are shown in Fig. 3f–i, all the elements such as Co, Zn, S, In are uniformly distributed in the composites, which is consistent with the expected result. These results prove that $ZnIn_2S_4$ and Co_3S_4 are intimately bound together, thus increasing the transfer and separation of photogenerated charge carriers and improving the photocatalytic performance.

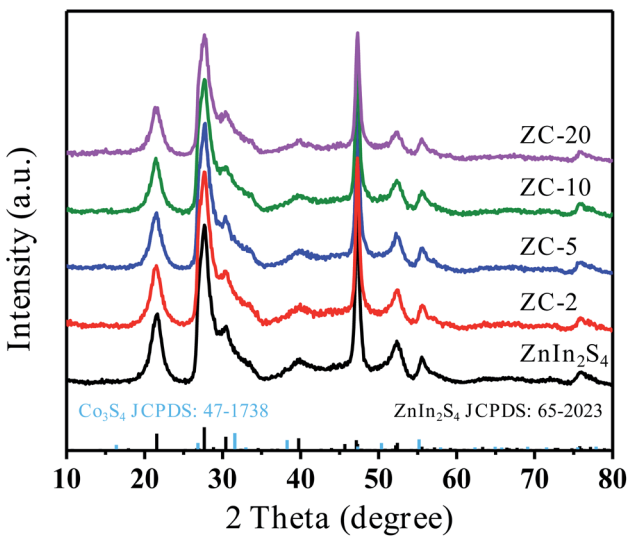

Fig. 1 XRD patterns of $ZnIn_2S_4$ and ZC-*X* (*X* = 2, 5, 10, 20) composites.

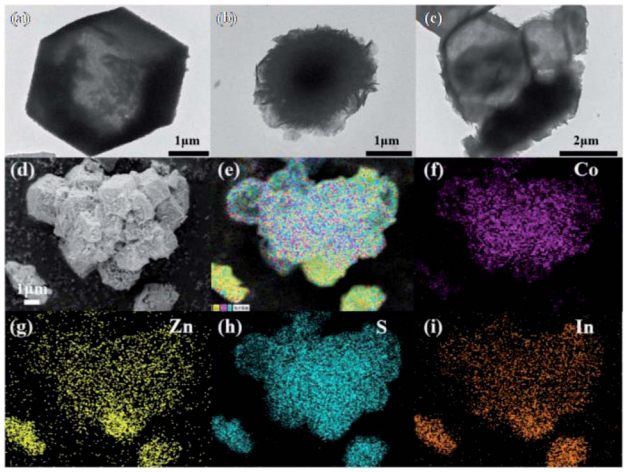

Fig. 2 TEM images of Co_3S_4 (a), $ZnIn_2S_4$ (b) and ZC-5 (c) SEM images of ZC-5 (d and e) elemental mappings of Zn (f), S (g), Co (h) and In (i) in ZC-5.

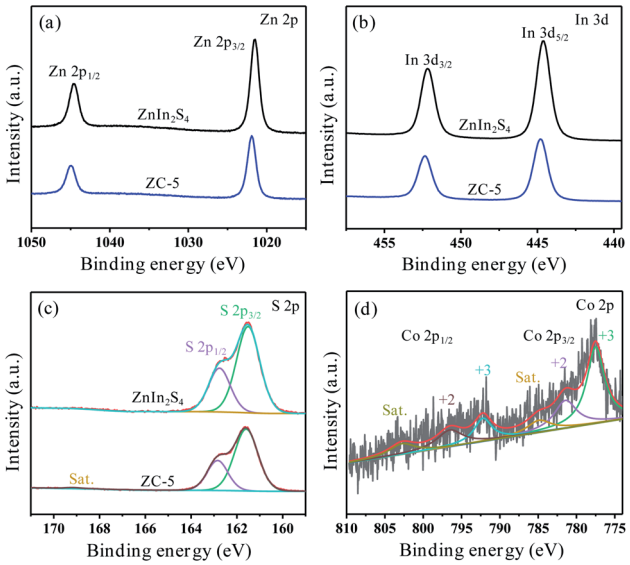

Fig. 3 XPS spectra of $ZnIn_2S_4$ and ZC-5: Zn 2p (a), In 3d (b), S 2p (c), Co 2p (d).

The BET specific surface area and porosity play important roles in evaluating the properties of prepared photocatalysts. The pore size distribution and nitrogen adsorption/desorption isotherm of $ZnIn_2S_4$ and ZC-5 samples are shown in Fig. S3.† It is evident that the two samples belong to mesoporous structure, owing to the IV adsorption isotherm with H_3 hysteresis loop.[40] The BET specific surface area of $ZnIn_2S_4$ and ZC-5 are 75.8 and 90.4 $m^2\ g^{-1}$, respectively. Obviously, the specific surface area of ZC-5 increases after the introduction of Co_3S_4. Meanwhile, the pore size of samples is mainly focus on 2.5–7.5 nm based on the Barrett–Joyner–Halenda (BJH) pore size distribution curves (the inset in Fig. S3†), which coincides with the conclusion of mesoporous structure obtained by isotherm curve.[41] Therefore, relatively large specific surface area and mesoporous structure can increase the reactive sites, which is beneficial to promote the photocatalytic hydrogen production.

The XPS measurements were introduced to further confirm the elemental composition and valence state of pure $ZnIn_2S_4$ and ZC-5. Meanwhile, the electron transfer mechanism supported heterojunction formation in ZC-5 can be explained by the comparison of XPS between our photocatalyst and pure counterpart. As shown in Fig. S4,† the survey XPS spectrum proves the existence of Zn, In, C and S in $ZnIn_2S_4$ and ZC-5, it is worth noting that C element comes from conductive resin. Fig. 3a shows the XPS spectrum of Zn 2p, including two prominent peaks at 1021.51 and 1044.57 eV, which correspond exactly to Zn $2p_{3/2}$ and Zn $2p_{1/2}$ in the $ZnIn_2S_4$, respectively.[42] However, the corresponding characteristic peaks of the Zn 2p in ZC-5 positive shifting is 1021.93 and 1044.98 eV. As displayed in Fig. 3b, the spectrum of In 3d in $ZnIn_2S_4$ shows two characteristic peaks at 444.61 and 452.18 eV which are assigned to In $3d_{5/2}$ and In $3d_{3/2}$, respectively.[42] The offset direction is similar to the above, with the peaks position of In 3d in ZC-5 located at 444.80 and 452.34 eV, respectively. For the S 2p (Fig. 3c), the XPS spectrum of $ZnIn_2S_4$ can be deconvoluted into two prominent peaks which situates at 161.51 and 162.75 eV, corresponding to the S $2p_{3/2}$ and S $2p_{1/2}$, respectively.[42] However, the peaks of S 2p in ZC-5 locate in the 161.60 and 162.84 eV. In addition, ZC-5 spectrum has one more characteristic peak at 169.09 eV compared with that of $ZnIn_2S_4$, which belongs to the vibration satellite peak existing in Co_3S_4.[43] It can be seen that the valence states of Zn, In and S are +2, +3 and −2, respectively. Meanwhile, the Co 2p XPS spectrum (Fig. 3d) contains two spin–orbit doublets peaks which are Co $2p_{3/2}$ and Co $2p_{1/2}$ and two satellites peaks. The fitting peaks at 777.51 and 792.15 eV are ascribed to Co^{3+}, and the peaks of Co^{2+} are located at 781.38 and 796.33 eV, as well as the vibration satellite peaks at 784.84 and 802.73 eV.[45] It proves that Co_3S_4 exists in $ZnIn_2S_4$. Meanwhile, compared with those of pure $ZnIn_2S_4$, the peak positions of Zn 2p, In 3d and S 2p in the ZC-5 sample positive shifting specifies the transfer of electrons from the $ZnIn_2S_4$ with a rich electron system to the Co_3S_4 with a poor electron system. The electron density of the $ZnIn_2S_4$ in the ZC-5 composite decreases, resulting in higher binding energy. Meanwhile, because of the electronegativity of Zn (1.65) and In (1.78) are lower than that of Co (1.88), which is further proved that the electron of $ZnIn_2S_4$ tends to transfer to more electronegative Co_3S_4. Therefore, $ZnIn_2S_4$ and Co_3S_4 are not simply physically mixed. From the above analysis, it can be proved the formation of heterogeneous structures with strong electronic interaction between $ZnIn_2S_4$ and Co_3S_4 in ZC-5.[44]

3.2. Light absorption properties

Fig. 4a shows the UV-vis diffuse reflection spectra (DRS) of $ZnIn_2S_4$, ZC-*X* ($X = 2$, 5, 10, 20) and Co_3S_4. As can be seen, the absorption edge of $ZnIn_2S_4$ is *ca.* 540 nm. In contrast, Co_3S_4 exhibits broad absorption in the range of 200–800 nm. Owing to the coupling of Co_3S_4, the visible light absorption of the ZC-*X* composites is significantly enhanced, meanwhile the absorption range also gradually widens with the increase of Co_3S_4 ratio. In accordance with the Tauc plot equation,[46] the band gap values of the prepared $ZnIn_2S_4$, ZC-*X* ($X = 2$, 5, 10, 20) and Co_3S_4 could be calculated as 2.55, 2.52, 2.51, 2.47, 2.46 and 1.62 eV, respectively (Fig. 4b), which proves that the band gap becomes narrow gradually with the increase of Co_3S_4 content in the composites. Therefore, the broader absorption range in the visible region arising from the coupling of Co_3S_4 play an

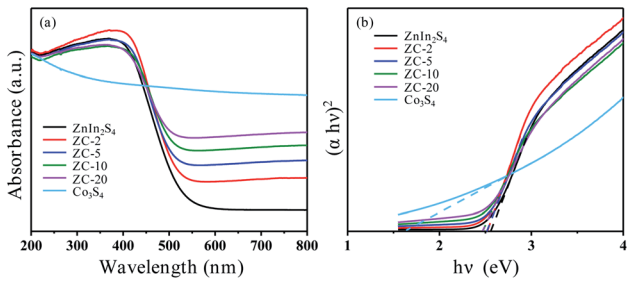

Fig. 4 UV-vis DRS of $ZnIn_2S_4$, Co_3S_4 and ZC-*X* composite photocatalysts (a) the plots to determine the band gaps for each sample (b).

important role in improving the photocatalytic performance of $ZnIn_2S_4$.

Ultraviolet photoelectron spectroscopy (UPS) is employed to determine the valence band energy (E_{VB}) of $ZnIn_2S_4$ ZC-5 and Co_3S_4, which are found to be 5.82, 6.03 and 5.1 eV *via* subtracting the width of the He I UPS spectra (Fig. S5†) from the excitation energy (21.2 eV). The valence band energy is subtracted from the band gap energy (E_g) to obtain the conduction band energy (E_{CB}), which are calculated to be 3.27, 3.52 and 3.48 eV, respectively. On the basis of the reference standard in which 0 V *vs.* RHE (reversible hydrogen electrode) equals −4.44 eV *vs.* evac (vacuum level), the E_{VB}, E_g and E_{CB} values of $ZnIn_2S_4$, ZC-5 and Co_3S_4 in electron volts can be changed into electrochemical energy potentials in volts.[47] Therefore, the valence band (VB) edge of $ZnIn_2S_4$ and ZC-5 can be observed at 1.38 and 1.59 V and that of Co_3S_4 is to be 0.66 V, the conduction band (CB) edge of $ZnIn_2S_4$, ZC-5 and Co_3S_4 are estimated to be −1.17, −0.92 and −0.96 V, respectively.

3.3. Charge-separation properties

Generally, photoluminescence (PL) spectrum is measured to provide information which is in connection with charge generation, transfer and recombination. The weaker emission peak means a lower electron–hole recombination rate. The PL spectrum of prepared $ZnIn_2S_4$ and ZC-*X* are shown in Fig. 5a. Compared with all prepared samples, the fluorescence emission intensity of ZC-5 is the lowest, which implies that the recombination of photogenerated electrons and holes is effectively inhibited on account of electron transfer between $ZnIn_2S_4$ and Co_3S_4, so as to improve photocatalytic activity. Furthermore, the photocurrent response and electrochemical impedance spectroscopy (EIS) are carried out to explain the separation and recombination of electron–hole pair and electron transfer by using pure $ZnIn_2S_4$ and ZC-*X* as the electrode, respectively. As displayed in Fig. 5b, $ZnIn_2S_4$ and ZC-*X* photoelectrodes show the relatively stable current response and the trend are consistent with the literature[12] under both dark and light conditions, but the saturation density of photocurrent is obviously different. It is clear that ZC-5 exhibits the highest photocurrent density when exposed to simulated sunlight, which is *ca.* 6.6 times of $ZnIn_2S_4$, suggesting that the photogenerated charges separation and transfer can be effectively promoted by combining with a certain amount of Co_3S_4, thus enhancing the photocatalytic hydrogen production effect. In addition, the electrochemical impedance spectroscopy (EIS) of prepared $ZnIn_2S_4$ and ZC-5 are depicted in Fig. 5c. Compared with $ZnIn_2S_4$, ZC-5 has a smaller radius, indicating that the electron transfer resistance of ZC-5 is lower, thus accelerating the electron transfer and inhibiting the charge recombination. Meanwhile, according to the photoluminescence spectrum, photocurrent response and electrochemical impedance spectroscopy of Co_3S_4 shown in Fig. S6,† the recombination rate of charge carriers on Co_3S_4 is relatively lower than $ZnIn_2S_4$. Consequently, the advantage of ZC-5 in preferably facilitating the effective separation of electron–hole pairs could improve photocatalytic activity.

In addition, Mott–Schottky measurements are employed to ensure the conduction band (CB) boundary of the synthesized photocatalysts. As displayed in Fig. S7a and b,† the slopes of the tangent line in the Mott–Schottky diagram are positive, implying that the pure $ZnIn_2S_4$ and ZC-5 belong to the n-type semiconductor.[48] At the same time, the flat-band potentials obtained by the *x*-axis intercepts can be approximated as the E_{CB} potentials.[49] It can be seen that the E_{CB} potential of ZC-5 is estimated to be −0.94 V *vs.* NHE and that of $ZnIn_2S_4$ is about −1.20 V *vs.* NHE, and Fig. S7c† displays the E_{CB} potential of Co_3S_4 which is estimated to be −0.93 V *vs.* NHE. All the results are almost consistent with the result of XPS valence band spectrum. The positive shift of ZC-5's E_{CB} potential may be due to the change of fermi energy level caused by the interaction between $ZnIn_2S_4$ and Co_3S_4.[22]

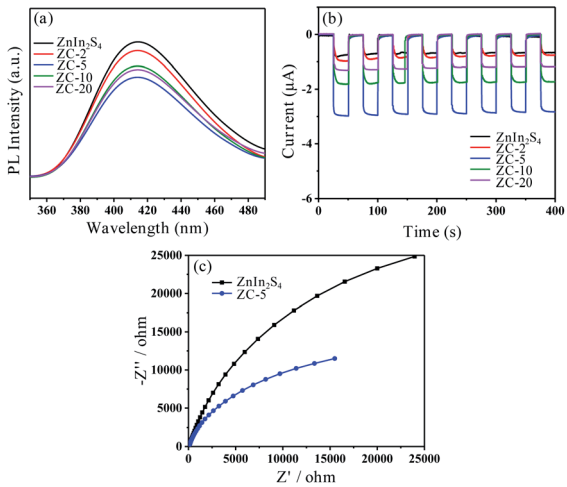

Fig. 5 Photo-luminescence (PL) spectra of $ZnIn_2S_4$ and prepared ZC-*X* composites (a) photocurrent–time curves of $ZnIn_2S_4$ and prepared ZC-*X* composites under the irradiation of simulated sunlight (b) Nyquist impedance plots of EIS for $ZnIn_2S_4$ and ZC-5 (c).

3.4. Photocatalytic performance and stability

The photocatalytic hydrogen production of prepared $ZnIn_2S_4$, ZC-*X* ($X = 2$, 5, 10, 20) and Co_3S_4 are tested by the irradiation of simulated sunlight. As can be seen from Fig. 6a, the hydrogen production of $ZnIn_2S_4$ and ZC-*X* increase steadily over time.

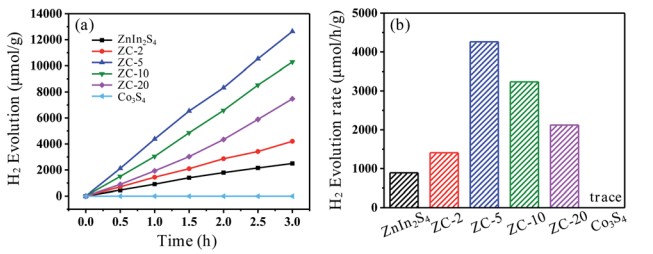

Fig. 6 The photocatalytic H_2 evolution performance over the synthesized $ZnIn_2S_4$ and ZC-*X* composites (a) the photocatalytic H_2 evolution rate of prepared $ZnIn_2S_4$ and ZC-*X* composite photocatalysts (b).

However, the hydrogen production of pure Co_3S_4 is difficult to be detected, which means that Co_3S_4 is inactive in photocatalytic hydrogen production. Meanwhile, as shown in Fig. 6b, when pure $ZnIn_2S_4$ is used as the photocatalyst, the production of hydrogen is merely 890 μmol g^{-1} h^{-1}, possibly due to the quenching of photogenerated charge carriers. In the presence of Co_3S_4, ZC-*X* composites show better photocatalytic activity. When the compound amount of Co_3S_4 increases to 5%, the hydrogen production rate reaches a maximum of 4261 μmol g^{-1} h^{-1} which is nearly 4.8 times than that of original $ZnIn_2S_4$. However, as the proportion of Co_3S_4 continues to increase, the photocatalytic activity of hydrogen evolution tends to decrease, which may be caused by excess Co_3S_4 blocking $ZnIn_2S_4$'s absorption of light.[23,50] In order to evaluate the stability of the photocatalyst, a cycle test was conducted. Obviously, after three cycles, there is no significant change in the amount of photocatalytic hydrogen produced by ZC-5 (Fig. S8a†). Meanwhile, the XRD patterns of ZC-5 is consistent before and after photocatalytic reactions (Fig. S8b†), suggesting that the crystal structure of ZC-5 shows no significant change. Therefore, ZC-5 composite has excellent reusability and photostability in hydrogen production as a photocatalyst.

4. Photocatalytic mechanism

According to the band gap and the position of the CB and VB of $ZnIn_2S_4$ and Co_3S_4, the possible photocatalytic hydrogen production reaction mechanism of $ZnIn_2S_4$@Co_3S_4 nanocomposites is proposed and exhibited in Fig. 7. $ZnIn_2S_4$ nanoparticles can be excited to produce photogenerated electrons and holes when exposed to simulated sunlight. Compared with other composites, the lower photocatalytic activity of pure $ZnIn_2S_4$ is due to the higher recombination rate of the generated electrons and holes. However, when Co_3S_4 and $ZnIn_2S_4$ are combined, the excited electrons are quickly transferred from the CB of $ZnIn_2S_4$ to that of Co_3S_4 because of the relatively lower CB position of $ZnIn_2S_4$. Therefore, the photogenerated electron–hole pairs recombination of $ZnIn_2S_4$ can be effectively inhibited. Since the E_{CB} potential of $ZnIn_2S_4$@Co_3S_4 is lower than the reduction potential of H^+/H_2, the photogenerated electrons accumulated on Co_3S_4 convert H^+ in the water to H_2 in a reduction reaction. Meanwhile, the photogenerated holes quickly transferred from the VB of $ZnIn_2S_4$ to that of Co_3S_4 on account of the E_{VB} potential of $ZnIn_2S_4$ is more positive than that of Co_3S_4. Moreover, the oxidation reactions will be further occurred, which react between sacrificial agents (TEOA) and the holes. Consequently, heterogeneous structures may be formed at the interface between $ZnIn_2S_4$ and Co_3S_4, which promote electron transfer and inhibit electron–hole pairs recombination, thus improving the photocatalytic hydrogen production activity of composites.

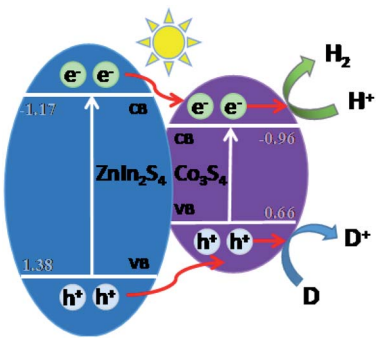

Fig. 7 Schematic illustration of the possible mechanism for photocatalytic hydrogen evolution over the $ZnIn_2S_4$@Co_3S_4 composite photocatalyst.

5. Conclusions

In summary, a series of $ZnIn_2S_4$@Co_3S_4 composite photocatalysts with certain structure are successfully carried out in photocatalytic hydrogen production under simulated sunlight. The three-dimensional Co_3S_4 samples are firstly obtained *via* solvothermal process and quenching of ZIF-67, then the coupling of obtained Co_3S_4 and $ZnIn_2S_4$ is achieved through a simple hydrothermal reaction. It is revealed that the $ZnIn_2S_4$@Co_3S_4 composite materials show better photocatalytic hydrogen production performance than pure $ZnIn_2S_4$, and the coupling amount of Co_3S_4 has a profound effect on the photocatalytic activity. From all synthesized samples, the ZC-5 composite possesses superior photocatalytic property with the hydrogen evolution rate of 4261 μmol g^{-1} h^{-1} which is approximately 4.8 times than that of pure $ZnIn_2S_4$ (890 μmol g^{-1} h^{-1}). The enhanced photocatalytic activity of ZC-5 may be attributed to the formation of heterostructure which promotes electron transfer and inhibits electron–hole pairs recombination, and the more active sites provided by the increased specific surface area. In addition, ZC-5 photocatalyst exhibits remarkable stability in photocatalytic hydrogen production performance. The working mechanism of $ZnIn_2S_4$@Co_3S_4 heterojunction is discussed in detail, which provides reference for the potential application of photocatalytic hydrogen production technology in the field of energy.

Conflicts of interest

There are no conflicts to declare.

Acknowledgements

The authors of this work gratefully appreciate the financial support provided by National Natural Science Foundation of China (No. 41573096, 21707064), Program for Changjiang Scholars and Innovative Research Team in University (No. IRT_17R71), Program for Professor of Special Appointment (Eastern Scholar) at Shanghai Institutions of Higher Learning (QD2019005).

Notes and references

1 Y. Li, Z. Jin, L. Zhang and K. Fan, *Chin. J. Catal.*, 2019, **40**, 390–402.

2 T. Huang, W. Chen, T.-Y. Liu, Q.-L. Hao and X.-H. Liu, *Int. J. Hydrogen Energy*, 2017, **42**, 12254–12261.
3 A. Kudo and Y. Miseki, *Chem. Soc. Rev.*, 2009, **38**, 253–278.
4 G. Colón, *Appl. Catal., A*, 2016, **518**, 48–59.
5 A. Fujishima and K. Honda, *Nature*, 1972, **238**, 37–38.
6 X. Chen, S. Shen, L. Guo and S. S. Mao, *Chem. Rev.*, 2010, **110**, 6503–6570.
7 J. Huo, L. Fang, Y. Lei, G. Zeng and H. Zeng, *J. Mater. Chem. A*, 2014, **2**, 11040–11044.
8 S. Yang, Y. Gong, J. Zhang, L. Zhan, L. Ma, Z. Fang, R. Vajtai, X. Wang and P. M. Ajayan, *Adv. Mater.*, 2013, **25**, 2452–2456.
9 Y. Wu, H. Wang, W. Tu, S. Wu, Y. Liu, Y. Z. Tan, H. Luo, X. Yuan and J. W. Chew, *Appl. Catal., B*, 2018, **229**, 181–191.
10 H. Tian, M. Liu and W. Zheng, *Appl. Catal., B*, 2018, **225**, 468–476.
11 Y. Pan, X. Yuan, L. Jiang, H. Yu, J. Zhang, H. Wang, R. Guan and G. Zeng, *Chem. Eng. J.*, 2018, **354**, 407–431.
12 A. Yan, X. Shi, F. Huang, M. Fujitsuka and T. Majima, *Appl. Catal., B*, 2019, **250**, 163–170.
13 S. Wang, B. Y. Guan and X. W. D. Lou, *J. Am. Chem. Soc.*, 2018, **140**, 5037–5040.
14 Z. Chen, D. Li, W. Zhang, Y. Shao, T. Chen, M. Sun and X. Fu, *J. Phys. Chem. C*, 2009, **113**, 4433–4440.
15 Z. Lei, W. You, M. Liu, G. Zhou, T. Takata, M. Hara, K. Domen and C. Li, *Chem. Commun.*, 2003, 2142–2143, DOI: 10.1039/b306813g.
16 X. Peng, L. Ye, Y. Ding, L. Yi, C. Zhang and Z. Wen, *Appl. Catal., B*, 2020, **260**, 118152.
17 X. Bai and J. Li, *Mater. Res. Bull.*, 2011, **46**, 1028–1034.
18 S. Shen, L. Zhao, Z. Zhou and L. Guo, *J. Phys. Chem. C*, 2008, **112**, 16148–16155.
19 C. Du, B. Yan, Z. Lin and G. Yang, *J. Mater. Chem. A*, 2020, **8**, 207–217.
20 S. Shen, L. Zhao, X. Guan and L. Guo, *J. Phys. Chem. Solids*, 2012, **73**, 79–83.
21 H. An, Z. Lv, K. Zhang, C. Deng, H. Wang, Z. Xu, M. Wang and Z. Yin, *Appl. Surf. Sci.*, 2021, **536**, 147934.
22 J. Zhou, D. Chen, L. Bai, L. Qin, X. Sun and Y. Huang, *Int. J. Hydrogen Energy*, 2018, **43**, 18261–18269.
23 L. Wei, Y. Chen, Y. Lin, H. Wu, R. Yuan and Z. Li, *Appl. Catal., B*, 2014, **144**, 521–527.
24 M. Zhang, J. Yao, M. Arif, B. Qiu, H. Yin, X. Liu and S.-m. Chen, *Appl. Surf. Sci.*, 2020, **526**, 145749.
25 H. Song, N. Wang, H. Meng, Y. Han, J. Wu, J. Xu, Y. Xu, X. Zhang and T. Sun, *Dalton Trans.*, 2020, **49**, 10816–10823.
26 S. Shen, L. Zhao and L. Guo, *J. Phys. Chem. Solids*, 2008, **69**, 2426–2432.
27 H. Liu, C. Xu, D. Li and H.-L. Jiang, *Angew. Chem., Int. Ed.*, 2018, **130**, 5477–5481.
28 G. Huang, Q. Yang, Q. Xu, S.-H. Yu and H.-L. Jiang, *Angew. Chem., Int. Ed.*, 2016, **128**, 7505–7509.
29 Y. Liu, W. Miao, X. Fang, Y. Tang, D. Wu and S. Mao, *Chem. Eng. J.*, 2020, **380**, 122584.
30 M. Wang, Z. Shen, X. Zhao, F. Duanmu, H. Yu and H. Ji, *J. Hazard. Mater.*, 2019, **371**, 352–361.
31 H. Xu, J. Cao, C. Shan, B. Wang, P. Xi, W. Liu and Y. Tang, *Angew. Chem., Int. Ed. Engl.*, 2018, **57**, 8654–8658.
32 D. P. Kumar, H. Park, E. H. Kim, S. Hong, M. Gopannagari, D. A. Reddy and T. K. Kim, *Appl. Catal., B*, 2018, **224**, 230–238.
33 N. Li, H. Huang, R. Bibi, Q. Shen, R. Ngulube, J. Zhou and M. Liu, *Appl. Surf. Sci.*, 2019, **476**, 378–386.
34 J.-T. Ren, K. Yuan, K. Wu, L. Zhou and Y.-W. Zhang, *Inorg. Chem. Front.*, 2019, **6**, 366–375.
35 S. Bala, I. Mondal, A. Goswami, U. Pal and R. Mondal, *J. Mater. Chem. A*, 2015, **3**, 20288–20296.
36 Z. F. Huang, J. Song, K. Li, M. Tahir, Y. T. Wang, L. Pan, L. Wang, X. Zhang and J. J. Zou, *J. Am. Chem. Soc.*, 2016, **138**, 1359–1365.
37 L. Xu, W.-q. Chen, S.-q. Ke, S.-m. Zhang, M. Zhu, Y. Zhang, W.-y. Shi, S. Horike and L. Tang, *Chem. Eng. J.*, 2020, **382**, 122810.
38 B. Liu, X. Liu, J. Liu, C. Feng, Z. Li, C. Li, Y. Gong, L. Pan, S. Xu and C. Q. Sun, *Appl. Catal., B*, 2018, **226**, 234–241.
39 F. Luo, D. Ma, Y. Li, H. Mi, P. Zhang and S. Luo, *Electrochim. Acta*, 2019, **299**, 173–181.
40 S. G. Mohamed, I. Hussain and J. J. Shim, *Nanoscale*, 2018, **10**, 6620–6628.
41 M. Thommes, K. Kaneko, A. V. Neimark, J. P. Olivier, F. Rodriguez-Reinoso, J. Rouquerol and K. S. W. Sing, *Pure Appl. Chem.*, 2015, **87**, 1051–1069.
42 X.-l. Li, X.-j. Wang, J.-y. Zhu, Y.-p. Li, J. Zhao and F.-t. Li, *Chem. Eng. J.*, 2018, **353**, 15–24.
43 Y. Guo, J. Tang, H. Qian, Z. Wang and Y. Yamauchi, *Chem. Mater.*, 2017, **29**, 5566–5573.
44 L. Ye, J. Fu, Z. Xu, R. Yuan and Z. Li, *ACS Appl. Mater. Interfaces*, 2014, **6**, 3483–3490.
45 S. Hou, Y. Lian, Y. Bai, Q. Zhou, C. Ban, Z. Wang, J. Zhao and H. Zhang, *Electrochim. Acta*, 2020, **341**, 136053.
46 J. Tauc, R. Grigorovici and A. Vancu, *Phys. Status Solidi B*, 1966, **15**, 627–637.
47 J. Liu, Y. Liu, N. Liu, Y. Han, X. Zhang, H. Huang, Y. Lifshitz, S.-T. Lee, J. Zhong and Z. Kang, *Science*, 2015, **347**, 970–974.
48 A. Wolcott, W. A. Smith, T. R. Kuykendall, Y. Zhao and J. Z. Zhang, *Adv. Funct. Mater.*, 2009, **19**, 1849–1856.
49 Y. Xia, Q. Li, K. Lv, D. Tang and M. Li, *Appl. Catal., B*, 2017, **206**, 344–352.
50 L. Bai, X. Cai, J. Lu, L. Li, S. Zhong, L. Wu, P. Gong, J. Chen and S. Bai, *ChemCatChem*, 2018, **10**, 2107–2114.